ARTICLE

Check for updates

Thermally stable quantum Hall effect in a gated ferroelectric-graphene heterostructure

Anubhab Dey[1], Nathan Cottam [1], Oleg Makarovskiy [1], Wenjing Yan[1], Vaidotas Mišeikis [2,3], Camilla Coletti [2,3], James Kerfoot[4], Vladimir Korolkov [4], Laurence Eaves[1], Jasper F. Linnartz[5], Arwin Kool[5], Steffen Wiedmann [5] & Amalia Patanè [1✉]

The quantum Hall effect is widely used for the investigation of fundamental phenomena, ranging from topological phases to composite fermions. In particular, the discovery of a room temperature resistance quantum in graphene is significant for compact resistance standards that can operate above cryogenic temperatures. However, this requires large magnetic fields that are accessible only in a few high magnetic field facilities. Here, we report on the quantum Hall effect in graphene encapsulated by the ferroelectric insulator $CuInP_2S_6$. Electrostatic gating of the graphene channel enables the Fermi energy to be tuned so that electrons in the localized states of the insulator are in equilibrium with the current-carrying, delocalized states of graphene. Due to the presence of strongly bound states in this hybrid system, a quantum Hall plateau is observed over a wide range of temperatures in relatively modest magnetic fields.

[1] School of Physics and Astronomy, University of Nottingham, Nottingham NG7 2RD, UK. [2] Center for Nanotechnology Innovation @NEST, Istituto Italiano di Tecnologia, Piazza San Silvestro 12, 56127 Pisa, Italy. [3] Graphene Labs, Istituto Italiano di Tecnologia, Via Morego, 30, 16163 Genova, Italy. [4] Park Systems UK Ltd, Medicity Nottingham, D6 Thane Road, Nottingham NG90 6BH, UK. [5] High Field Magnet Laboratory (HFML –EMFL), Radboud University, Toernooiveld 7, 6525 ED Nijmegen, The Netherlands. ✉email: amalia.patane@nottingham.ac.uk

The electronic properties of graphene are very sensitive to applied magnetic fields (**B**) and are ideally suited for the investigation of the quantum Hall effect (QHE). This is exemplified by plateaus in the Hall resistance due to the quantization of the two-dimensional electron motion into Landau levels (LL)[1–9]. The QHE, first discovered in Si metal–oxide–semiconductor field-effect transistors[10], exhibits important differences in graphene due to the electron–hole degeneracy near the charge neutrality point, which leads to a distinctive half-integer QHE and a non-zero Berry's phase of the electron wavefunction[4,5,7–9].

Of particular significance for the QHE in graphene is the effect of dopant impurities near its surface. Screening effects in graphene[11,12] tend to be weakened by a magnetic field and can facilitate the localization of charge carriers in the disordered potential of the graphene layer[13,14]. For example, for epitaxial graphene on a Si-terminated SiC substrate[15–18], donors reside in the SiC layer adjacent to the graphene layer. These dopants act as a reservoir of electrons for graphene, maintaining the Hall voltage on the $\nu = 2$ QH plateau over a wide range of magnetic fields[19]. An extended quantum Hall plateau was also observed in graphene-based field effect transistors (FETs) in which graphene is capped by a thin layer of the van der Waals crystal InSe[20,21]. These examples of "giant" QH plateaus in graphene have been reported at low temperatures ($T < 200$ K) and have been assigned to the magnetic field and electric field induced transfer of charge carriers between the degenerate LLs of graphene and the localized states in its proximity. A full microscopic model for the QHE in these hybrid systems does not yet exist. However, recent work has modeled the interaction between free carriers and localized charges near the surface of graphene[22], showing that when the chemical potential is in the gap between LLs, these charges can form stable bound states over a distance of the order of the magnetic length $l_B = \sqrt{\hbar/eB}$ and with binding energy $E_B \approx \hbar v_F / l_B$, where $v_F \approx 10^6$ m/s is the Fermi velocity and e is the elementary charge. This phenomenon can persist well beyond cryogenic temperatures, opening possibilities for the manipulation of the QHE at room temperature. To date, a room temperature resistance quantum has been reported only in high mobility graphene at large magnetic fields that are available only in a few high field magnet laboratories[5,23].

Here, we report on the QHE in FETs based on a single layer graphene channel capped with the insulating ferroelectric van der Waals crystal $CuInP_2S_6$ (CIPS). The CIPS layer acts as a source of localized charge carriers in proximity to graphene. We report a hysteretic behavior in the longitudinal and transverse magnetoresistance of graphene over a range of applied magnetic fields and temperatures. Similar hysteretic phenomena in the resistivity of graphene have been reported in zero magnetic field and assigned to charge trapping[24–29] and/or ferroelectric polarization[30–34]. In this work, we report on the dynamic exchange of charge carriers at the CIPS/graphene interface and its influence on the QHE and its hysteretic behavior. The QHE is found to be weakly dependent on temperature over a range of easily accessible magnetic fields.

Results

Transport characteristics in zero magnetic field. The CIPS/graphene heterostructure was prepared by exfoliation and viscoelastic stamping of a CIPS flake on a Hall bar based on high-quality graphene grown by CVD (chemical vapor deposition). Figure 1a shows the optical image of a ten-terminal Hall bar, half of which is based on graphene (G) and the other half on CIPS/graphene (CG), mounted on a 285 nm-thick SiO_2/n-Si substrate. The morphology of the layers was probed by atomic force
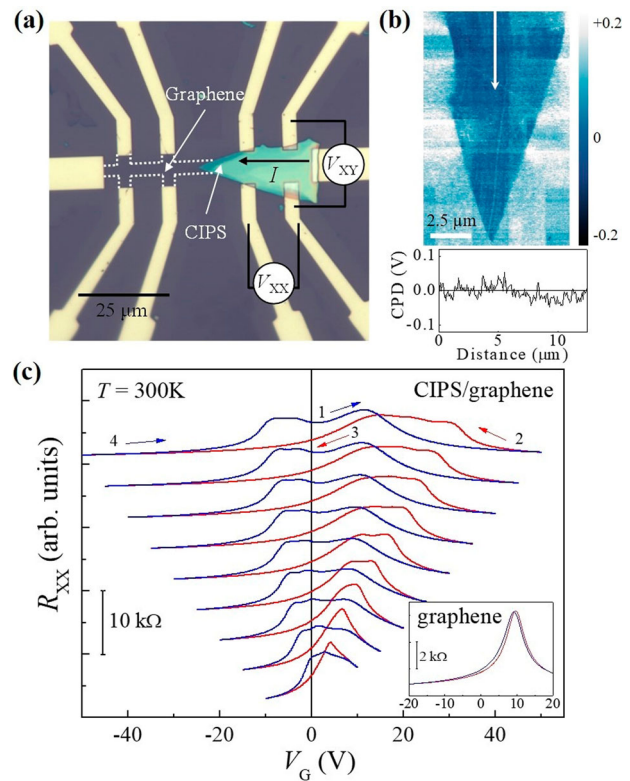

Fig. 1 Gated Hall bar based on graphene capped with CuInP₂S₆. a Optical image of a Hall bar based on CuInP$_2$S$_6$/graphene (CG) on a SiO$_2$/n-Si substrate and Ni-Au contacts. One section of the graphene layer is covered by a CIPS layer. The white dotted lines mark the edges of pristine graphene. **b** Amplitude-modulated Kelvin probe force microscopy (AM-KPFM) contact potential difference (CPD) map and CPD profile of CIPS/graphene measured with a Multi75E cantilever at a voltage amplitude of $V_{AC} = 4$ V and frequency $f_{AC} = 17$ kHz. The CPD-profile is obtained along the length of the CIPS-flake, as indicated by the white arrow in the map. **c** Resistance-gate voltage $R_{XX}(V_G)$ curves for CG at $T = 300$ K ($I = 1\,\mu$A, $B = 0$ T). The sweep up/down branches are shown in blue and red arrows, respectively. Curves are displaced along the vertical axis for clarity. Inset: $R_{XX}(V_G)$ curve for a reference sample based on pristine graphene at $T = 300$ K ($I = 1\,\mu$A, $B = 0$ T). This sample corresponds to the uncapped section of the graphene Hall bar shown in part (**a**). A sweep rate $\Delta V_G/\Delta t = 0.3$ V/s was used for the measurements.

microscopy (AFM) and single pass amplitude-modulated Kelvin probe force microscopy (AM-KPFM)[35]. The CIPS layer has a non-uniform thickness ranging from 20 to 50 nm and a uniform work function potential at the graphene/CIPS interface (Fig. 1b). Details of the fabrication and of the characterization of the CIPS flakes by AFM and piezoresponse force microscopy (PFM) are presented in the experimental section, Supplementary Note 1 and Supplementary Fig. 1.

The longitudinal resistance R_{XX} was measured at a constant current ($I = 1\,\mu$A). The voltage drop V_{XX} across different pairs of terminals along the graphene channel was measured over a range of gate voltages V_G applied between the graphene and Si-gate electrodes. As can be seen in the inset of Fig. 1c, for pristine graphene the $R_{XX}(V_G)$ curve at $T = 300$ K is peaked at the neutrality point $V_{NP} = +10$ V. Using a capacitance model of the graphene FET, we estimate a hole density $p = 7 \times 10^{11}$ cm^{-2} at $V_G = 0$ and a hole (electron) mobility $\mu = 9 \times 10^3$ cm^2/Vs (1×10^4 cm^2/Vs) for carrier concentrations in the range 10^{11}–10^{12} cm^{-2} at $T = 300$ K.

In contrast to pristine graphene, the $R_{XX}(V_G)$ curves for CIPS/graphene (CG) show a pronounced hysteresis and are asymmetric (Fig. 1c): The amplitude of the hysteresis increases with increasing the sweep range of V_G from $\Delta V_G = \pm 10$ V to ± 50 V. For $\Delta V_G = \pm 10$ V, the $R_{XX}(V_G)$ curves shift to lower V_G compared to pristine graphene; also, the field effect (and Hall) mobility for holes and electrons is reduced from $\mu \sim 10^4$ cm²/Vs to $\mu \sim 2 \times 10^3$ cm²/Vs. In general, the $R_{XX}(V_G)$ curve consists of multiple peaks, suggestive of a channel with a non-uniform distribution of dopants; also, the temporal response of R_{XX} is slow (with rise and decay times $\tau > 100$ s). Thus, the $R_{XX}(V_G)$ curve depends on the sweep range of V_G and sweep rate $\Delta V_G/\Delta t$. A value of $\Delta V_G/\Delta t = 0.3$ V/s was used for the data presented in this work.

Hysteresis in the transport characteristics of graphene can arise from a gate-induced polarization at the interface of graphene with a ferroelectric layer[33]. For our CG, the hysteresis is not dominated by this phenomenon as a gate-induced ferroelectricity would produce a shift of the neutrality point V_{NP} in the direction of the gate sweep, i.e., V_{NP} would shift to higher voltages when V_G is swept from negative to positive values compared to when V_G is swept from positive to negative values. On the other hand, a hysteresis can also originate from a slow charge transfer at the CIPS/graphene interface, as reported earlier in a similar device structure[25]. The gate voltage induces charges in the graphene layer, which then redistribute between the graphene and CIPS layers. In the first part of the sweep of V_G to positive gate voltages ($V_G > 0$ V), electrons are transferred from graphene onto CIPS; during the reverse sweep with $V_G < 0$ V, the CIPS layer discharges its electrons onto graphene. A non-homogeneous distribution of localized states in CIPS can create areas of graphene with different carrier densities, thus causing the multiple peaks in $R_{XX}(V_G)$ shown in Fig. 1c.

We model the hysteresis in $R_{XX}(V_G)$ using a classical capacitance model of the FET that takes into account a charge transfer across the CIPS/graphene interface (Supplementary Note 2 and Supplementary Fig. 2). We estimate that a charge ΔQ redistributes slowly between the graphene (Q_g) and CIPS (Q_{CIPS}) layers with a characteristic time constant $\tau > 100$ s; different regions of CG tend to charge/discharge with similar temporal dynamics; also, the value of $\Delta Q/e = n_Q$ is dependent on V_G and reaches values of up to $n_Q \sim 10^{12}$ cm⁻² at large V_G ($V_G = +50$ V) and $T = 300$ K.

The hysteresis in $R_{XX}(V_G)$ weakens with decreasing T (Fig. 2a) or under excitation of the sample with photons of energy ($h\nu = 3.06$ eV) larger than the band gap of CIPS (Supplementary Note 3 and Supplementary Fig. 3). Light of increasing intensity induces a shift of the neutrality point to larger positive V_G and a narrowing of the $R_{XX}(V_G)$ curve. This indicates that carriers photocreated in the CIPS layer can screen the disordered potential created by localized charges. In summary, the transport characteristics of graphene are very sensitive to charges transferred from/to the CIPS layer. This effect is observed in all our CG devices and is used to probe the role of localized charges on the QHE.

Magneto-transport and quantum Hall effect. Figure 2a, b show the temperature dependence of the $R_{XX}(V_G)$ curves for CG at $B = 0$ T and 16 T, respectively. At low temperatures ($T \leq 200$ K), the hysteresis in $R_{XX}(V_G)$ is weak, as also observed in the pristine graphene. However, it becomes pronounced for $T > 200$ K. In particular, in a magnetic field ($B = 16$ T in Fig. 2b), the $R_{XX}(V_G)$ curves exhibit additional maxima and minima. To illustrate this behavior more clearly, we plot in Fig. 2c–e the color maps of R_{XX} versus V_G and B at different T and for different (up/down) sweeps

of V_G. For T up to 200 K (Fig. 2c, d), the bright red region in $R_{XX}(B, V_G)$ centered at $V_{NP} \sim +30$ V corresponds to the neutrality point of graphene represented by the zeroth Landau level, LL ($n = 0$). For both sweep up/down branches, secondary peaks in $R_{XX}(B, V_G)$ emerge for $B > 5$ T at around $V_G = +20$ V and $+40$ V. As V_G increases from negative to positive values, first holes ($V_G < V_{NP}$) and then electrons ($V_G > V_{NP}$) fill successive LLs.

The energy-level spectrum of Dirac fermions in a magnetic field is described by the relation $E_n = \text{sgn}(n)\sqrt{2e\hbar v_F^2 B|n|}$, where $n = 0, 1, 2\ldots$ The spectrum comprises electron and hole LLs, as well as a LL ($n = 0$) at the neutrality point. We use the capacitance equation $C = e[dn_g/dV_G]$ to calculate the voltage separation ΔV_G of the maxima in $R_{XX}(V_G)$ at different B. Here $C = \varepsilon\varepsilon_0/t$ is the "classical" capacitance per unit area of the graphene/SiO₂/Si heterostructure, $t = 285$ nm is the SiO₂ layer thickness, $\varepsilon = 3.9$ is the relative dielectric constant of SiO₂, ε_0 is the permittivity of free space, and n_g is the carrier density in the graphene layer. We express the separation between the two maxima in $R_{XX}(V_G)$ corresponding to the alignment of the Fermi level with the $n = 0$ and $n = 1$ LLs as $\Delta V_G = eg/C$, where $g = 4eB/h$. This model reproduces the data at low T for both sweep up and down of V_G ($T = 4$ K and 200 K in Fig. 2c, d, white dashed lines), but fails to describe the data at $T > 200$ K ($T = 300$ K in Fig. 2e, white dashed lines). At $T = 300$ K, the LL quantization is obscured by a large hysteresis; in particular, the neutrality point V_{NP} shifts to larger positive V_G with increasing B. The black lines in Fig. 2e describe the deviation of the LL features in $R_{XX}(B, V_G)$ from a conventional LL chart model. The measured deviation is reproduced by considering a B-dependent charge transfer and the capacitance equation $C = e[dn_g/dV_G]$. The magnetic field tends to reduce the density of electrons transferred from CIPS to graphene by $\Delta n_g = 4 \times 10^{10}$ cm⁻² at $B = 10$ T and $\Delta n_g = 4 \times 10^{11}$ cm⁻² at $B = 16$ T. This phenomenon can also be seen in the dependence of the Hall resistance R_{XY} on B, V_G and T, as discussed below.

Figure 3a shows the V_G-dependence of R_{XY} over a range of temperatures ($T = 4–300$ K) and magnetic fields from $B = 0$ T to 16 T. Figure 3b compares the $R_{XY}(V_G)$ and $R_{XX}(V_G)$ curves at $B = 16$ T for different T. At $T = 4$ K (Fig. 3a,b, i), the $R_{XY}(V_G)$ curve shows QH plateaus centered at $V_G \approx +20$ V and $V_G \approx +40$ V, corresponding to the LL filling factor $\nu = 2$ for holes and electrons, respectively. Here, ν is derived from the relation $\nu = \pm 4(|n| + 1/2)$, where n is the LL index[16]. Plateaus corresponding to lower value of R_{XY} can also be seen at $V_G \approx -2$ V ($\nu = 6$) and $V_G \approx -25$ V ($\nu = 10$). As the temperature increases to $T = 100$ K (Fig. 3a, b-ii) and 200 K (Fig. 3a, b-iii), the QH plateaus tend to narrow. A further increase of temperature to $T \geq 300$ K (Fig. 3a, b-iv) induces a large hysteresis in the $R_{XY}(V_G)$ curves (see also Supplementary Notes 4, 5, 6 and Supplementary Figs. 4, 5, 6). Figure 4 shows the color plots of R_{XY} versus V_G and B at $T = 300$ K for different (up/down) sweeps of V_G. These data illustrate the sign of the $\nu = 2$ QH plateau and its evolution with increasing values of B and V_G. It can be seen that the neutrality point V_{NP} shifts to larger positive V_G with increasing B.

From Fig. 3 it can be seen that the $\nu = 2$ QH plateau is accompanied by a hysteresis that depends on T and B. This behavior is shown in more detail in Fig. 5a where the $R_{XY}(V_G)$ curves are plotted at $B = 16$ T for different T. Increasing T above $T = 100$ K causes a shift of the neutrality point V_{NP} to lower V_G, corresponding to an increasing density of electrons in the graphene layer. This behavior is not observed in pristine graphene and is assigned to the thermal excitation of electrons from CIPS into the graphene layer. For lower T ($T = 4.2$ and 100 K), the shift
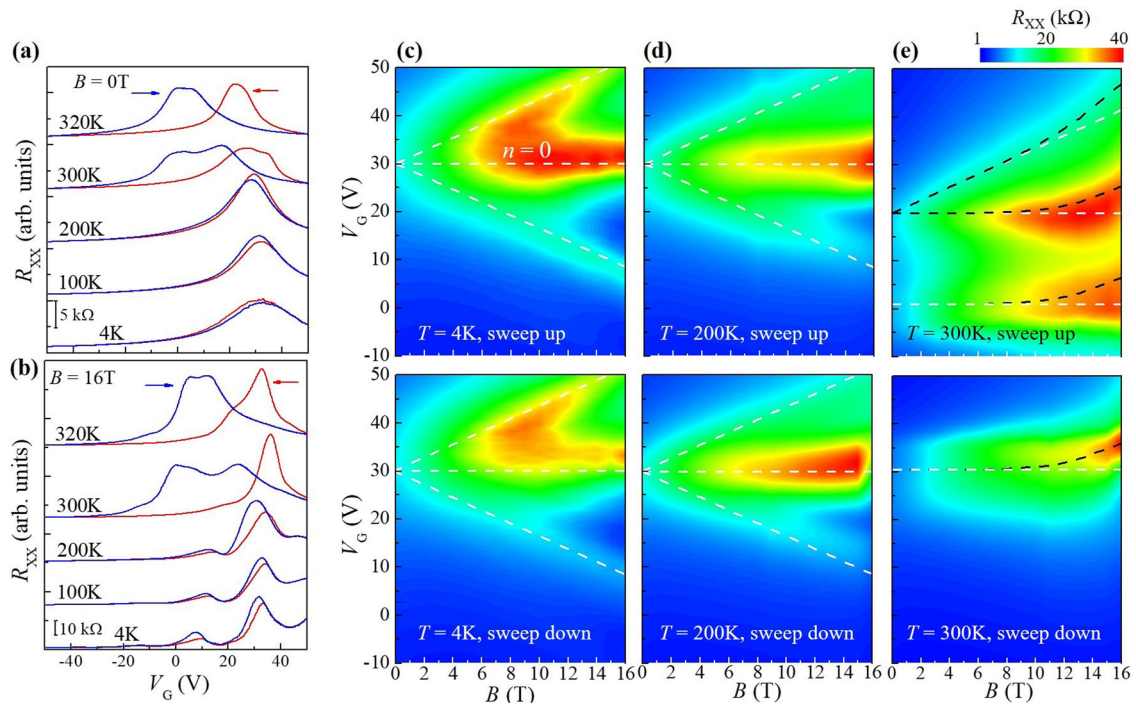
Fig. 2 Longitudinal magnetoresistance for CuInP₂S₆/graphene. a, b Resistance-gate voltage $R_{XX}(V_G)$ curves for CuInP₂S₆ (CIPS)/graphene at different temperatures T ($I = 1\,\mu A$) and for magnetic fields (**a**) $B = 0$ T and (**b**) $B = 16$ T. The sweep up/down branches are shown in blue and red, respectively. For clarity, curves are displaced along the vertical axis. Color plots of R_{XX} versus B and gate voltage V_G at (**c**) $T = 4$ K, (**d**) $T = 200$ K and (**e**) $T = 300$ K and different sweeps ($I = 1\,\mu A$). Dashed white lines represent the calculated Landau level (LL) charts using a conventional model, as described in the text. Dashed black lines in part (**e**) show the calculated LL charts assuming a B-dependent charge transfer.

of V_{NP} is towards higher values of V_G with increasing T, indicative of a thermal excitation of carriers near the Dirac point.

To quantify the hysteresis in $R_{XY}(V_G)$, we consider the gate voltage at which $R_{XY}(V_G)$ goes to zero (i.e., the charge neutrality point) on the sweep up (V_{Gu}) and sweep down (V_{Gd}) branches of $R_{XY}(V_G)$. The difference, $\left|\Delta V_{GH}\right| = \left|V_{Gu} - V_{Gd}\right|$, is shown in Fig. 5b. For $T < 200$ K, $\left|\Delta V_{GH}\right|$ is weakly dependent on T and increases with B. For $T > 200$ K, the hysteresis is more pronounced and is described by the relation $\left|\Delta V_{GH}\right| \propto \exp(-E_a/kT)$, where E_a is an activation energy ($E_a \approx 0.16$ eV for $B = 16$ T, Arrhenius plot in the inset of Fig. 5b). Also, from the T-dependence of $R_{XX}(V_G)$ on the $\nu = 2$ QH plateau, we extract an activation energy $E_{a-\nu2} = 0.05$ eV and 0.09 eV for the sweep up and down branches of $R_{XX}(V_G)$ (see Supplementary Fig. 6).

Due to the hysteresis and slow charge transfer in CG, the measurement of R_{XX} and R_{XY} versus B at a given V_G require special consideration. For each measurement of the $R_{XY}(B)$ and $R_{XX}(B)$ curves, the value of V_G was increased by small increments ($\Delta V_G/\Delta t = 0.1$ V/s) starting from $V_G = 0$ V until reaching the required value of V_G. The temporal dependence of R_{XY} and R_{XX} at $B = 0$ T was then followed over intervals of several minutes, as required for R_{XY} and R_{XX} to reach stable values. The magnetic field was then swept from $B = 0$ T to 16 T (sweep rate of 5 mT/s). The values of V_G were selected according to the $R_{XY}(V_G)$ curves in Figs. 3 and 4, showing plateaus on each side of the neutrality point (between the $n = 0$ and $n = \pm 1$ LLs) due to holes ($V_G \approx +20$ V) or electrons ($V_G \approx +40$ V).

Figure 6a shows the $R_{XY}(B)$ curves of CG for $V_G = +20$ V at $T = 4$ K and 300 K. It can be seen that the $R_{XY}(B)$ curves exhibit a weak T-dependence; in particular, the approach to the $\nu = 2$ QH plateau shifts to lower B-fields at $T = 300$ K. We have observed similar behaviors in other CG devices (Supplementary Note 7 and Supplementary Figs. 7, 8, 9), although the threshold in B for the

$\nu = 2$ QH plateau may differ depending on the quality of the graphene layer, which can contain defects introduced during the CVD-growth and/or the transfer of graphene from the Cu onto the SiO₂/Si substrate. The behavior of CIPS/graphene contrasts with the strong temperature dependence of the $\nu = 2$ QH plateau in pristine graphene (Fig. 6b, Supplementary Note 8, and Supplementary Fig. 10).

As shown in Figs. 4, 6c, d, we can select gate voltages at which a QH plateau is observed in CG for both holes and electrons. The plateau in $R_{XY}(B)$ is accompanied by a corresponding decrease in $R_{XX}(B)$ (Fig. 6e, Supplementary Note 9, and Supplementary Figs. 11–12). However, R_{XX} does not go to zero at values of B corresponding to the $\nu = 2$ QH plateau; also, R_{XY} deviates from its nominal quantized value ($h/2e^2$). As shown in Fig. 6f(i), (ii), this deviation (ΔR_{XY}) tends to zero for decreasing R_{XX}. Here, values of R_{XX} and R_{XY} are obtained from measurements of the same device at different T, B and/or V_G after the onset of the $\nu = 2$ QH plateau in $R_{XY}(B)$. These data indicate a coupling between R_{XX} and R_{XY} that could be accounted for by disorder. A non-uniform channel can exhibit regions that do not have minimal resistance at the same value of B, leading to an effective misalignment of the Hall probes so that R_{XY} is influenced by R_{XX}[36]. In particular, disorder can play an important role on the $\nu = 2$ QH plateau due to the contribution to the transport of both electrons and holes[37]. Using the data in Fig. 6f, we estimate the coupling parameter $s = \Delta R_{XY}/R_{XX}$. A linear fit of ΔR_{XY} versus R_{XX} gives $s = 0.04$ (0.05) at $T = 300$ K (4.2 K), similar to the value ($s = 0.038$) reported for graphene/SiC devices in the literature[38], although our values of ΔR_{XY} and R_{XX} are larger.

Discussion

The room temperature QHE was first reported in graphene and explained in terms of the magnetic field quantization of Dirac
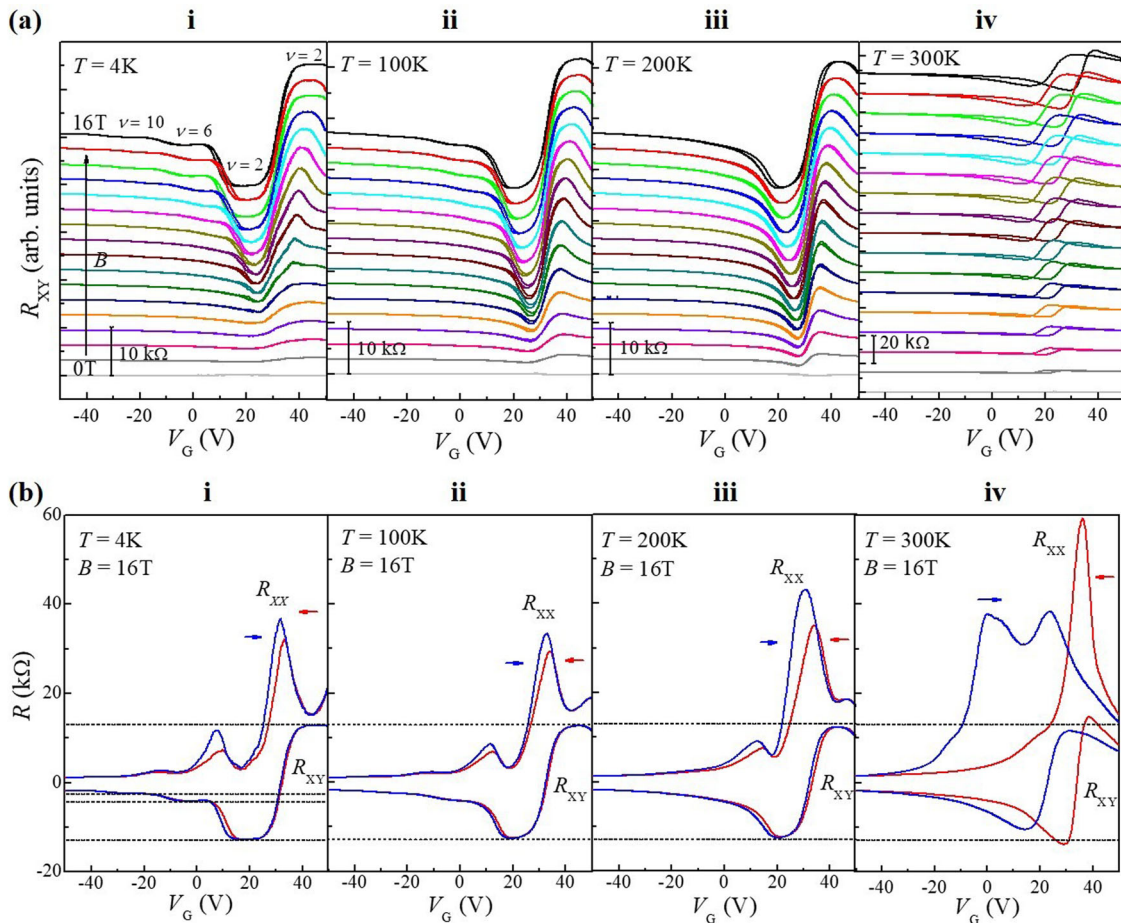
Fig. 3 Hall resistance for CuInP$_2$S$_6$/graphene. a Hall resistance-gate voltage $R_{XY}(V_G)$ curves for CuInP$_2$S$_6$/graphene at different temperatures: (i) $T = 4$ K, (ii) $T = 100$ K, (iii) $T = 200$ K, (iv) $T = 300$ K, and magnetic field B ranging from $B = 0$ T to 16 T in 1 T steps ($I = 1$ μA). **b** Longitudinal resistance R_{XX} and Hall resistance R_{XY} versus gate voltage V_G at $B = 16$ T and (i) $T = 4$ K, (ii) $T = 100$ K, (iii) $T = 200$ K, (iv) $T = 300$ K. Dashed lines correspond to the quantized values of R_{XY}.
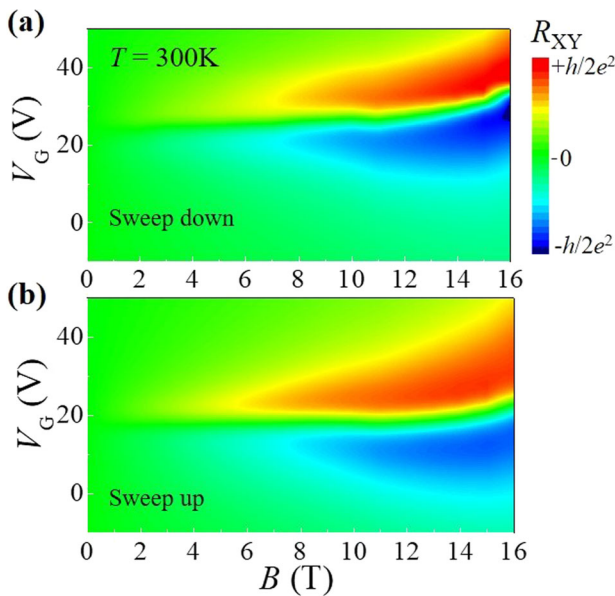

Fig. 4 Room temperature Hall resistance for CuInP$_2$S$_6$/graphene. Color plots of the Hall resistance R_{XY} for CuInP$_2$S$_6$/graphene versus magnetic field B and gate voltage V_G at temperature $T = 300$ K (current $I = 1$ μA) for (**a**) sweep down and (**b**) sweep up of V_G. The color bar indicates the value of R_{XY} and its quantized value ($h/2e^2$).

fermions in graphene[5]. The LL quantization energy of fermions in magnetic field is $E_n = v_F \sqrt{2e\hbar B |n|}$. For $n = \pm 1$ and $B = 45$ T, $E_n \sim 250$ meV, which greatly exceeds the thermal energy (~ 26 meV) of charge carriers at $T = 300$ K. However, the measured thermal activation energy E_a for the quenching of the $\nu = 2$ QH plateau in graphene corresponds to the cyclotron energy gap $E_1 = v_F \sqrt{2e\hbar B}$ only at high magnetic fields ($B \approx 30$ T), but it is smaller at lower B[39]. At high B, the number of states with zero energy ($n = 0$ LL) is determined by the total magnetic flux and does not depend on disorder. Thus, the $n = 0$ LL is well separated from its neighboring ($n = \pm 1$) LLs; in contrast, for lower B, LL mixing due to disorder broadens the LLs, leading to $E_a < E_1$[39]. Thus, the observation of the $\nu = 2$ QH plateau at room temperature in graphene requires a large B accessible only in a few high field facilities. In our CIPS/graphene sample the $\nu = 2$ QH plateau is observed at relatively small B over a wide range of temperatures, yet it is not seen in pristine graphene in the same range of B. This observation merits further consideration.

First, we note that the CIPS layer is a dielectric that acts as a source of disorder for graphene via charge transfer across the CIPS/graphene interface, which is tuneable by gating and is temperature dependent. Regions of CIPS with different densities of localized states tend to charge and discharge with a similar slow (~ 100 s) time constant at room temperature, thus accounting for the gate-induced hysteresis in the transport characteristics (Fig. 1c). The hysteresis is significant at $T > 200$ K (Fig. 2), symptomatic of a thermally activated transfer of charges from/to
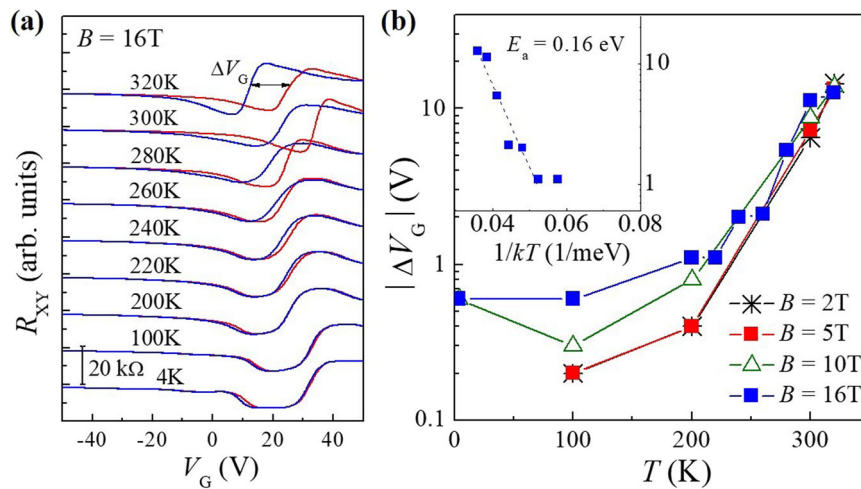
Fig. 5 Hysteresis in the Hall resistance of CuInP$_2$S$_6$/graphene. a Hall resistance $R_{XY}(V_G)$ for CuInP$_2$S$_6$/graphene at magnetic field $B = 16$ T and different temperatures T. The sweep up/down branches are shown in blue and red, respectively. For clarity, curves are displaced along the vertical axis (current $I = 1\,\mu$A). ΔV_{GH} is the amplitude of the hysteresis in $R_{XY}(V_G)$. **b** Amplitude of the hysteresis $|\Delta V_{GH}|$ versus T at different B. Lines are guides to the eye. For $T = 4.2$ K and $B \leq 5$ T, $|\Delta V_{GH}| \approx 0$. Inset: Arrhenius plot of $|\Delta V_{GH}|$ versus $1/T$ at $B = 16$ T. The dashed line is an exponential fit to the data.
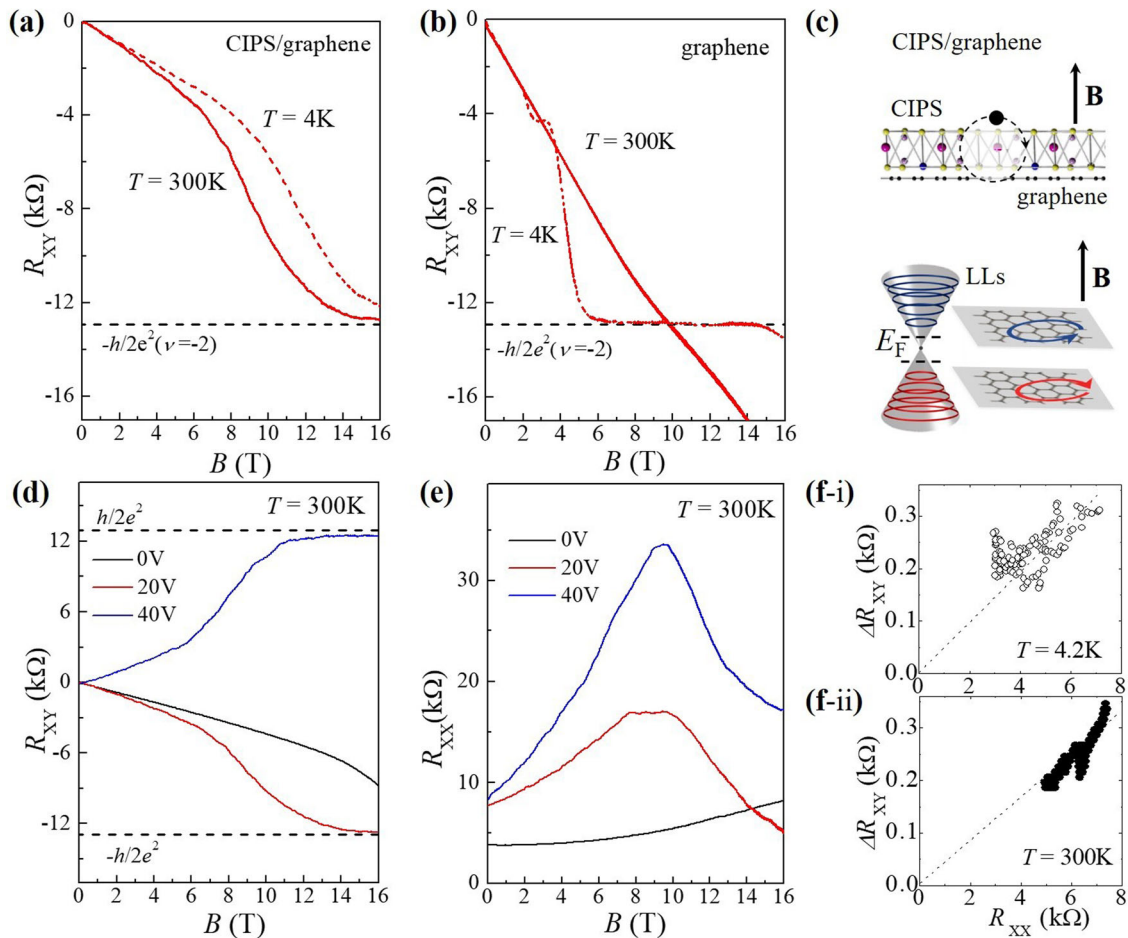

Fig. 6 Quantum Hall plateau in CuInP$_2$S$_6$/graphene. Hall resistance R_{XY} versus magnetic field B at temperatures $T = 4$ K and 300 K in (**a**) CuInP$_2$S$_6$/graphene (gate voltage $V_G = +20$ V and current $I = 1\,\mu$A) and (**b**) pristine graphene ($V_G = +3$ V, $I = 1\,\mu$A). **c** Top: Schematic of bound states in CuInP$_2$S$_6$/graphene. Bottom: Landau levels (LLs) in graphene with Fermi level aligned between the $n = 0$ and $n = 1$ LLs corresponding to the $v = 2$ quantum Hall plateau. **d** R_{XY} versus B for CuInP$_2$S$_6$/graphene at different V_G and $T = 300$ K ($I = 1\,\mu$A). Negative and positive values of R_{XY} refer to hole and electron resistivity, respectively. **e** R_{XX} versus B for CuInP$_2$S$_6$/graphene at different V_G and $T = 300$ K ($I = 1\,\mu$A). **f** Deviation of R_{XY} from the quantized value ($R_{XY} = h/2e^2$) versus R_{XX}, as derived from measurements at different T, B and V_G: (i) $T = 4.2$ K, $B = 16$ T, $V_G = 42-28$ V and 16–22 V; (ii) $T = 300$ K, $B = 14-16$ T, $V_G = 20$ V. Dashed lines are guides to the eye.

the CIPS layer onto graphene. A comparison of the transfer characteristics and the hysteresis for CG at $B = 0$ and 16 T indicates that the charge transfer across the CIPS/graphene interface is influenced by magnetic field. The magnetic field acts to enhance the hysteretic behavior and distorts the V_G-dependence of R_{XX} and R_{XY} around the charge neutrality point. As shown in Figs. 2e and 4, for $B \geq 10$ T the color regions in R_{XX} and R_{XY} corresponding to the zeroth LL tend to shift to larger V_G with increasing B, consistent with a reduced transfer of electrons from the CIPS layer onto graphene due to an increased localization of charges in the quantizing magnetic field. This can also be seen in Fig. 5b, where the hysteresis, as measured by $|\Delta V_{GH}|$, increases with B.

Reference [22] offers an insight into the role of localized charges near the surface of graphene: For a range of chemical potentials inside the gap between the zeroth and first LLs, charged impurities can form stable "molecules" bound by free carriers of opposite sign within graphene[22]. The optimal distance between charges in the bound state is of the order of the magnetic length $l_B = \sqrt{\hbar/eB}$ and their binding energy scales as $E_B = \hbar v_F/l_B$. For $B = 16$ T, this gives $l_B = 6.4$ nm and $E_B = 0.10$ eV. This binding energy is comparable to the activation energy of the T-dependent hysteresis in R_{XY} (Fig. 5b) and to the effective LL activation energy gap obtained from the T-dependence of R_{XX} (Supplementary Fig. 6). We note that a strongly disordered system cannot show the QHE because no LL quantization can occur. However, it is well established that the standard picture of the QHE requires the existence of disorder and localized states. This enables the Fermi level to be pinned at energies between the extended states of adjacent LLs. The presence of disorder is a key feature of the QHE and its thermal stability: it acts to pin the Fermi level at the localized states between the LLs and maintains the Hall voltage on the plateaus. The charge transfer between CIPS and graphene is reversible, leading to the $\nu = 2$ QH plateau for both electrons and holes, as shown in Figs. 4 and 6.

We now consider our findings in the context of ongoing research on other hybrid systems based on graphene. For example, the use of a conducting layer, such as the relatively small band gap semiconductor InSe ($\sim$1.3 eV at $T = 300$ K) to form an InSe/graphene FET, facilitates the observation of a giant QH plateau, but its observation at room temperature is prevented by parallel conduction in the InSe layer[20,21]. The use of a high-resistance dielectric poses other challenges. A giant QH plateau has been reported in graphene grown epitaxially by thermal annealing of a SiC dielectric substrate. In this case, the charge transfer across the SiC/graphene interface involves defects in SiC with a high densities of states (10^{14} cm^{-2} eV^{-1}) in close proximity to graphene[15–19]. These states arise from atomic-scale defects within the top few SiC layers, which are created during the formation of the graphene layer by Si-sublimation. For graphene on SiC, the giant QH effect was reported at temperatures of up to $T \sim 100$–200 K, suggesting that the bound states in SiC/graphene have a relatively small binding energy even at high B (>20 T). Alternatively, hexagonal boron nitride (hBN) represents an ideal dielectric for graphene-based FETs[40]. Charge and surface fluctuations in hBN tend to be weaker than in other substrates, such as SiO$_2$. Thus, graphene on hBN has a high-mobility and is well suited for observations of integer and fractional QHE[41,42]. In particular, the formation of moiré superlattices in rotationally misaligned graphene/hBN layers can promote interfacial charge transfer and new quantum transport regimes[43–46]. More recently, a hybrid system based on CrOCl-graphene revealed an exotic QH effect phase due to the formation of a long-wavelength charge ordering[47]. In all these different hybrid systems, the band structure of graphene is modified

around the Dirac cone as a result of an interfacial charge transfer involving a semiconductor or an insulator. However, for all these systems the observation of quantum effects at high temperatures has proven to be challenging. Our choice of CIPS provides an effective layer for charge transfer as CIPS is a dielectric and its defect states are not only sufficiently dense ($\sim$10^{12} cm^{-2} eV^{-1}), but also they form bound states that are sufficiently deep to be resilient to thermal ionization. The high temperatures ($T > 200$ K) for charge transfer and hysteresis in the transport curves corresponds to that required for activating the thermal motion of the Cu-ions[48,49] out of the CIPS layer planes. The slow motion of localized ionic charges could be responsible for the slow dynamics of charge transfer at the graphene/CIPS interface, leading to the hysteretic transport observed in this system. Since CIPS is a dielectric and electrons remain bound onto its localized states, the QH voltage in graphene is not short-circuited by a significant parallel conduction in CIPS.

In conclusion, the controlled transfer of charges between graphene and localized states in its proximity provides a route for the observation of the QHE over a wide range of temperatures and in readily accessible magnetic fields. The electric field-induced transfer of charge between the CIPS and graphene layers acts to increase or decrease the carrier density in graphene, causing a change in its resistance that is gate-tuneable. The charge transfer causes hysteretic behavior in the electrical characteristics due a slow dynamic exchange of electrons between graphene and localized states in its proximity. Prospects for further research include a more accurate resistance quantization, which will require progress in both material growth and fabrication processes. This requires high-mobility homogenous graphene, a homogenous charge transfer at the graphene/CIPS interface, and the fabrication of low-resistance contacts. A more uniform CIPS/graphene heterostructure could be achieved by the development of scalable growth techniques (for example using epitaxial graphene grown with intrinsic structural alignment on SiC) together with the fabrication of high-quality electrical contacts, such as electrodes with the edge-contact geometry[50]. Thus, there are prospects for further studies and for engineering interfacial charge transfer in hybrid systems based on graphene for the observation of quantum effects over a wide parameter space beyond the current state-of-the-art for future applications, such as graphene-based resistance standards[51].

Methods

Materials and device fabrication. The CuInP$_2$S$_6$ crystal was purchased from HQ Graphene. Graphene Hall bars were fabricated at the NEST laboratories at the Istituto Italiano di Tecnologia, Pisa, Italy. The fabrication of high-mobility CVD-grown graphene Hall bars before the deposition of CIPS is crucial for the observation of the QHE. Single-crystal graphene used in this work was grown on Cu foil by CVD in a cold-wall reactor (Aixtron BM Pro) using chromium nucleation seeds[52]. Graphene crystals were electrochemically delaminated from the growth substrate in 1 M NaOH and deposited on SiO$_2$/n-doped Si wafers using semi-dry transfer[53]. The fabrication of the Hall bars was carried out using e-beam lithography (20 kV, Raith Multibeam on Zeiss Ultra Plus scanning electron microscope). The graphene Hall bars were prepared using reactive ion etching (gas flow 80 sccm O$_2$ and 5 sccm Ar, RF power 35 W) and electrical contacts were deposited by thermal evaporation of 7 nm of Ni and 60 nm of Au. A Poly(methyl methacrylate) (PMMA) resist (950 K, 4.5% in anisole, Allresist) was used for lithography, followed by 2-step cleaning in acetone and removal of AR600-71 (Allresist) to ensure a polymer-free surface of graphene[54]. The wafer containing the

graphene Hall bar devices was covered with a protective coating of PMMA for dicing and storage. The processed wafers were diced into ~4×4 mm^2 chips and then cleaned in hot acetone ($T \sim 65\ ^\circ$C) for 1 h, rinsed with isopropyl alcohol (IPA) and dried with pressurized nitrogen gas to remove the protective PMMA coating. These devices were then annealed in a tube furnace at $T = 300\ ^\circ$C for 3 h in a 5% H$_2$ and 95% Ar flowing gas atmosphere to remove surface impurities and residues on the graphene surface. The graphene was then used for stamping the CIPS layer to form the CIPS/graphene heterostructure. The interface between graphene and CIPS after stamping was not further cleaned. The heterostructure was fabricated by exfoliating a CIPS flake onto polydimethylsiloxane (PDMS) from a low-residue tape and identified using optical microscopy. By using a micro-manipulator stage, an exfoliated flake of CIPS on PDMS was aligned to one section of the graphene Hall bar and brought into contact with it. The PDMS was then slowly retracted in order to deposit CIPS. The graphene Hall bar capped with CIPS was bonded into non-magnetic chip carriers for electrical measurements.

Optical, electrical and microscopy studies. The surface topography of the flakes was acquired by atomic force microscopy (AFM, Park NX20) in non-contact mode under ambient conditions. The KPFM study was conducted using an additional lock-in amplifier connected to the same AFM system. Transport measurements in the dark and under light illumination were conducted in vacuum (2×10^{-6} mbar) using Keithley-2400 source-meters and Keithley-2010 multi-meters. A temperature controller from Lakeshore Cryotronics was used to control and probe the temperature. A solid-state laser ($\lambda = 405$ nm) and a He-Ne laser ($\lambda = 632.8$ nm) were used for the optical studies. The position of the laser spot was adjusted on the device and measurements were taken at different powers. A cryogen free magnet (Cryogenic Limited) was used to perform the magneto-transport studies over a range of temperatures.

Data availability

The data that support the findings of this study are available from the corresponding author upon reasonable request.

References

1. Goerbig, M. O. Electronic properties of graphene in a strong magnetic field. *Rev. Mod. Phys.* **83**, 1193–1243 (2011).
2. Slizovskiy, S. & Betouras, J. J. Nonlinear magnetization of graphene. *Phys. Rev. B* **86**, 125440 (2012).
3. Castro Neto, A. H., Guinea, F., Peres, N. M. R., Novoselov, K. S. & Geim, A. K. The electronic properties of graphene. *Rev. Mod. Phys.* **81**, 109–162 (2009).
4. Zhang, Y. B., Tan, Y. W., Stormer, H. L. & Kim, P. Experimental observation of the quantum hall effect and Berry's phase in graphene. *Nature* **438**, 201–204 (2005).
5. Novoselov, K. S. et al. Room-temperature quantum hall effect in graphene. *Science* **315**, 1379–1379 (2007).
6. Kane, C. L. & Mele, E. J. Quantum spin Hall effect in graphene. *Phys. Rev. Lett.* **95**, 226801 (2005).
7. Gusynin, V. P. & Sharapov, S. G. Unconventional integer quantum Hall effect in graphene. *Phys. Rev. Lett.* **95**, 146801 (2005).
8. Guinea, F., Katsnelson, M. I. & Geim, A. K. Energy gaps and a zero-field quantum Hall effect in graphene by strain engineering. *Nat. Phys.* **6**, 30–33 (2010).
9. Novoselov, K. S. et al. Unconventional quantum hall effect and Berry's phase of 2 pi in bilayer graphene. *Nat. Phys.* **2**, 177–180 (2006).
10. Vonklitzing, K., Dorda, G. & Pepper, M. New method for high-accuracy determination of the fine-structure constant based on quantized hall resistance. *Phys. Rev. Lett.* **45**, 494–497 (1980).
11. Fogler, M. M., Novikov, D. S. & Shklovskii, B. I. Screening of a hypercritical charge in graphene. *Phys. Rev. B* **76**, 233402 (2007).
12. Terekhov, I. S., Milstein, A. I., Kotov, V. N. & Sushkov, O. P. Screening of Coulomb impurities in graphene. *Phys. Rev. Lett.* **100**, 076803 (2008).
13. Luican-Mayer, A. et al. Screening charged impurities and lifting the orbital degeneracy in graphene by populating landau levels. *Phys. Rev. Lett.* **112**, 036804 (2014).
14. Pyatkovskiy, P. K. & Gusynin, V. P. Dynamical polarization of graphene in a magnetic field. *Phys. Rev. B* **83**, 075422 (2011).
15. Alexander-Webber, J. A. et al. Phase space for the breakdown of the quantum hall effect in epitaxial graphene. *Phys. Rev. Lett.* **111**, 096601 (2013).
16. Janssen, T. J. B. M. et al. Anomalously strong pinning of the filling factor nu=2 in epitaxial graphene. *Phys. Rev. B* **83**, 233402 (2011).
17. Kopylov, S., Tzalenchuk, A., Kubatkin, S. & Fal'ko, V. I. Charge transfer between epitaxial graphene and silicon carbide. *Appl. Phys. Lett.* **97**, 112109 (2010).
18. Tzalenchuk, A. et al. Towards a quantum resistance standard based on epitaxial graphene. *Nat. Nanotechnol.* **5**, 186–189 (2010).
19. Alexander-Webber, J. A. et al. Giant quantum hall plateaus generated by charge transfer in epitaxial graphene. *Sci. Rep.* **6**, 30296 (2016).
20. Kudrynskyi, Z. R. et al. Giant quantum hall plateau in graphene coupled to an InSe van der Waals Crystal. *Phys. Rev. Lett.* **119**, 157701 (2017).
21. Bhuiyan, M. A. et al. Photoquantum hall effect and light-induced charge transfer at the interface of Graphene/InSe heterostructures. *Adv. Funct. Mater.* **29**, 1805491 (2019).
22. Slizovskiy, S. Bound states of charges on top of graphene in a magnetic field. *Phys. Rev. B* **92**, 195426 (2015).
23. Vaquero, D. et al. Phonon-mediated room-temperature quantum Hall transport in graphene. *Nat. Commun.* **14**, 318 (2023).
24. Wang, H. M., Wu, Y. H., Cong, C. X., Shang, J. Z. & Yu, T. Hysteresis of electronic transport in graphene transistors. *Acs Nano* **4**, 7221–7228 (2010).
25. Dey, A. et al. Memristive effects due to charge transfer in graphene gated through ferroelectric CuInP2S6. *2D Mater.* **9**, 035003 (2022).
26. Kalon, G., Shin, Y. J., Truong, V. G., Kalitsov, A. & Yang, H. The role of charge traps in inducing hysteresis: capacitance-voltage measurements on top gated bilayer graphene. *Appl. Phys. Lett.* **99**, 083109 (2011).
27. Yusuf, M. H., Nielsen, B., Dawber, M. & Du, X. Extrinsic and intrinsic charge trapping at the graphene/ferroelectric interface. *Nano Lett.* **14**, 5437–5444 (2014).
28. Liao, Z. M., Han, B. H., Zhou, Y. B. & Yu, D. P. Hysteresis reversion in graphene field-effect transistors. *J. Chem. Phys.* **133**, 044703 (2010).
29. Choi, M. S. et al. Controlled charge trapping by molybdenum disulphide and graphene in ultrathin heterostructured memory devices. *Nat. Commun.* **4**, 1624 (2013).
30. Hwang, H. J., Lee, S. K., Kim, S. M. & Lee, B. H. Direct measurement of transient charging and dipole alignment speed in Ferroelectric Hf0.5Zr0.5O2 Gate dielectric using graphene FETs. *Adv. Electron. Mater.* **7**, 2100145 (2021).
31. Rajapitamahuni, A., Hoffman, J., Ahn, C. H. & Hong, X. Examining graphene field effect sensors for ferroelectric thin film studies. *Nano Lett.* **13**, 4374–4379 (2013).
32. Wan, S. Y. et al. Nonvolatile ferroelectric memory effect in ultrathin -In2Se3. *Adv. Funct. Mater.* **29**, 1808606 (2019).
33. Zheng, Y. et al. Graphene field-effect transistors with ferroelectric gating. *Phys. Rev. Lett.* **105**, 16602 (2010).
34. Lipatov, A. et al. Polarization-dependent electronic transport in Graphene/Pb(Zr,Ti)O-3 ferroelectric field-effect transistors. *Adv. Electron. Mater.* **3**, 1700020 (2017).
35. Nonnenmacher, M., Oboyle, M. P. & Wickramasinghe, H. K. Kelvin probe force microscopy. *Appl. Phys. Lett.* **58**, 2921–2923 (1991).
36. Hartland, A. The quantum hall-effect and resistance standards. *Metrologia* **29**, 175–190 (1992).
37. Poumirol, J. M., Escoffier, W., Kumar, A., Raquet, B. & Goiran, M. Impact of disorder on the v=2 quantum Hall plateau in graphene. *Phys. Rev. B* **82**, 121401 (2010).
38. Chae, D. H. et al. Investigation of the stability of graphene devices for quantum resistance metrology at direct and alternating current. *Meas. Sci. Technol.* **33**, 065012 (2022).
39. Giesbers, A. J. M. et al. Quantum-hall activation gaps in graphene. *Phys. Rev. Lett.* **99**, 206803 (2007).
40. Dean, C. R. et al. Boron nitride substrates for high-quality graphene electronics. *Nat. Nanotechnol.* **5**, 722–726 (2010).
41. Yang, W. et al. Epitaxial growth of single-domain graphene on hexagonal boron nitride. *Nat. Mater.* **12**, 792–797 (2013).
42. Ponomarenko, L. A. et al. Cloning of Dirac fermions in graphene superlattices. *Nature* **497**, 594–597 (2013).

43. Woods, C. R. et al. Commensurate-incommensurate transition in graphene on hexagonal boron nitride. *Nat. Phys.* **10**, 451–456 (2014).

44. Finney, N. R. et al. Tunable crystal symmetry in graphene-boron nitride heterostructures with coexisting moire superlattices. *Nat. Nanotechnol.* **14**, 1029–1034 (2019).

45. Hunt, B. et al. Massive Dirac Fermions and Hofstadter Butterfly in a van der Waals Heterostructure. *Science* **340**, 1427–1430 (2013).

46. Yankowitz, M. et al. Emergence of superlattice Dirac points in graphene on hexagonal boron nitride. *Nat. Phys.* **8**, 382–386 (2012).

47. Wang, Y. et al. Quantum Hall phase in graphene engineered by interfacial charge coupling. *Nat. Nanotechnol.* **17**, 1272–1279 (2022).

48. Balke, N. et al. Locally controlled Cu-Ion transport in layered Ferroelectric CuInP2S6. *ACS Appl. Mater. Interfaces* **10**, 27188–27194 (2018).

49. Neumayer, S. M. et al. Ionic control over Ferroelectricity in 2D Layered van der Waals capacitors. *ACS Appl. Mater. Interfaces* **14**, 3018–3026 (2022).

50. Wang, L. et al. One-dimensional electrical contact to a two-dimensional material. *Science* **342**, 614–617 (2013).

51. He, H. et al. Accurate graphene quantum Hall arrays for the new International System of Units. *Nat. Commun.* **13**, 6933 (2022).

52. Miseikis, V. et al. Deterministic patterned growth of high-mobility large-crystal graphene: a path towards wafer scale integration. *2D Mater.* **4**, 021004 (2017).

53. Giambra, M. A. et al. Wafer-scale integration of graphene-based photonic devices. *Acs Nano* **15**, 3171–3187 (2021).

54. Tyagi, A. et al. Ultra-clean high-mobility graphene on technologically relevant substrates. *Nanoscale* **14**, 2167–2176 (2022).

Acknowledgements

Author contributions

A.P. and A.D. conceived the project and wrote the paper; C.C and V.M. fabricated the graphene Hall bars; A.D. fabricated the CIPS/graphene devices and performed the transport studies assisted by N.C., O.M. and A.P.; A.D. conducted the analysis of the data, assisted by A.P. and O.M.; J.K. and V.K. conducted the microscopy studies; W.Y. and L.E. contributed to the transport studies of CIPS and their analysis in zero magnetic field; C.C. and V.M. synthesized and transferred single-crystal CVD graphene and fabricated the graphene Hall bars; J.F.L., A.K. and S.W. contributed to the transport studies in high magnetic fields at the EMFL; all authors discussed the results.

Competing interests

The authors declare no competing interests.

Additional information

Supplementary information The online version contains supplementary material available at https://doi.org/10.1038/s42005-023-01340-8.

Correspondence and requests for materials should be addressed to Amalia Patanè.

Peer review information *Communications Physics* thanks the anonymous reviewers for their contribution to the peer review of this work.

Reprints and permission information is available at http://www.nature.com/reprints

Publisher's note Springer Nature remains neutral with regard to jurisdictional claims in published maps and institutional affiliations.